arXiv:cond-mat/0304571v1 [cond-mat.mes-hall] 25 Apr 2003

Impurity and spin effects on the magneto-spectroscopy of a THz-modulated nanostructure

Vidar Gudmundsson* and Chi-Shung Tang
Physics Division, National Center for Theoretical Sciences, P.O. Box 2-131, Hsinchu 30013, Taiwan

Andrei Manolescu
Science Institute, University of Iceland, Dunhaga 3, IS-107 Reykjavik, Iceland

We present a grid-free DFT model appropriate to explore the time evolution of electronic states in a semiconductor nanostructure. The model can be used to investigate both the linear and the nonlinear response of the system to an external short-time perturbation in the THz regime. We use the model to study the effects of impurities on the magneto-spectroscopy of a two-dimensional electron gas in a nanostructure excited by an intense THz radiation. We do observe a reduction in the binding energy of the impurity with increasing excitation strength, and at a finite magnetic field we find a slow onset of collective spin-oscillations that can be made to vanish with a stronger excitation.

I. INTRODUCTION

The interest in the properties of radiation induced excited states in bulk semiconductors,[1,2] or a two-dimensional electron gas (2DEG),[3] and semiconductor nanostructures[4] has grown in the last years parallel to advances in high precision experimental techniques and sample making skills. Increased brilliance of coherent far-infrared (THz) synchrotron radiation[5] and sensitive photoconductivity measurements techniques[1,2] will certainly intensify research activities on electronic systems driven far from equilibrium and time-dependent phenomena in nanostructures.

We model and investigate here the time evolution of a short nanoscale quantum wire or an elongated quantum dot with one embedded impurity after the system with several electrons has been irradiated by a short intense THz pulse. Corresponding atomic systems have been investigated,[6] but the present model of an artificial two-dimensional (2D) molecule in a GaAs structure allows us to consider the effects of an external magnetic field $B < 2$ T, that is commonly available in the labs and has large effects on the 2DEG in a AlGaAs/GaAs heterostructure, but very small effects on usual atomic systems.

Having seen that an intensive THz pulse can cause nonlinear effects in quantum dots[7] and rings[8] and possibly change the binding energy of impurities in bulk material[2] we study its effects in the present system on the binding energy of the impurity in presence of other interacting electrons, and ask ourselves if it is possible to excite collective spin modes in the system in an external magnetic field. THz radiation with the equivalent energy of few meV is simply on an appropriate scale with the energy spectrum of our system determined by its geometry (finite size) and the host material of GaAs.

Modeling time-dependent phenomena in nanosystems in a magnetic field driven out of equilibrium does not leave many options to a researcher. The Coulomb interaction between the electrons is usually of paramount interest together with the spin structure of the system. This can be emphasized by its finite size even though the effective g-factor may be small as is the case in GaAs. The well established time-dependent Hartree-Fock approximation can be adequate in many cases,[7] but one would hope for more accurate spin structure delivered by a time-dependent local spin-density approximation (LSDA).[9] It has to be kept in mind that both the inclusion of the magnetic field in a LSDA[10] and its extensions to dynamic systems[11] are nontrivial tasks and are not fully completed to date. In our approach we shall use the ground state parameterization of the exchange and correlation functionals and ignore the small corrections due to current terms in the functionals in a magnetic field.[12]

Commonly, both in calculations for excited atoms and molecules[6,13,14] or nanostructures,[7,9] a spatial grid has been employed. In this work we resort to recently developed grid-free implementation of LSDA[15,16,17,18] in the hope to be able to describe complex dynamical systems for a longer period of time. The grid-free methods, as will become clear below, result in the transformation of the relevant equations to compact matrix equations of not too large size. On the other hand the matrix elements are usually much more complicated than in grid methods, even though most of them are known analytically. This compact matrix structure of the problem lends itself very well to the matrix and vector handling of modern computer languages and facilitates parallelization that does neither require lare bandwidth nor high communication speed between the nodes of a CPU cluster.

II. MODEL

A. The ground state

To calculate the time evolution of the system requires the knowledge of the initial state, its ground state, at a particular time $t = t_0$, which within the LSDA is de-

scribed by the Kohn-Sham equations

$$H|\alpha) = (H_0 + H_\sigma + V_\phi + H_{\rm int})\,|\alpha) = \varepsilon_\alpha|\alpha), \quad (1)$$

where H_0 is the Hamiltonian for the 2DEG in the perpendicular magnetic field $\mathbf{B} = B\hat{\mathbf{z}}$, that is confined by the parabolic potential $V_{\rm conf}(r) = m^*\omega_0^2 r^2/2$. A more general shape of the system is attained through the additional confinement potential V_ϕ breaking the rotational symmetry of H_0 and modifying the radial confinement

$$V_\phi(\mathbf{r}) = \frac{1}{2}m^*\omega_0 r^2 \sum_{p=1}^{p_{\rm max}} \alpha_p \cos(p\varphi) + V_0 \exp(-\gamma r^2), \quad (2)$$

where $p_{\rm max}$ is an even integer to ensure confinement. The eigenstates $|\alpha\rangle$ of the Fock-Darwin[19] Hamiltonian H_0 are used as a mathematical basis in which the eigenstates $|\alpha)$ of H are expanded, as a result Eq. (1) can be transformed into a matrix eigenvalue equation. A suitable truncation of the basis $\{|\alpha\rangle\}$, that can be varied to improve the accuracy, then leads to a numerically tractable eigenvalue problem.

In this LSDA mean-field type of an approximation the effective interaction $H_{\rm int}$ is composed of the direct Coulomb repulsion potential, or the Hartree term

$$V_{\rm H}(\mathbf{r}) = \frac{e^2}{\kappa}\int \frac{n(\mathbf{r}')}{|\mathbf{r}-\mathbf{r}'|}d\mathbf{r}', \quad (3)$$

and the potential describing the effects of the exchange and correlation

$$V_{xc,\sigma}(r,B) = \frac{\partial}{\partial n_\sigma}(n\epsilon_{xc}[n_\uparrow, n_\downarrow, B])|_{n_\sigma = n_\sigma(r)}, \quad (4)$$

where $n_\sigma(r)$ is one of the two spin ($\sigma = \uparrow, \downarrow$) components of the total electron density $n = n_\uparrow + n_\downarrow$. The Zeeman energy of the electrons is included in H_σ with the appropriate effective g-factor g^* and the Bohr magneton, μ_B, $H_\sigma = \pm(1/2)g^*\mu_B B$.

In a large 2DEG the natural length and energy scales are the magnetic length $l = \sqrt{\hbar c/(eB)}$ and the cyclotron energy $\hbar\omega_c = \hbar eB/(m^*c)$, and instead of the electron density it is convenient to define the local filling factor $\nu(\mathbf{r}) = 2\pi l^2 n(\mathbf{r})$. In the confined system described by H_0 the appropriate length scale is $a = l\sqrt{\omega_c/\Omega}$, an "effective magnetic length", where $\Omega = \sqrt{\omega_c^2 + 4\omega_0^2}$ is the new characteristic frequency of the system. We shall thus use a modified filling factor appropriate for a finite system

$$\tilde{\nu}(\mathbf{r}) = 2\pi a^2 n(\mathbf{r}), \quad (5)$$

and the polarization $\zeta(\mathbf{r}) = [n_\uparrow(\mathbf{r}) - n_\downarrow(\mathbf{r})]/n(\mathbf{r})$ as new variables to express the exchange and correlation potentials (4) in. This will allow us to have a unified description of the system in a finite or vanishing magnetic field.

In these new variables the exchange and correlation potentials are[20]

$$V_{xc,\uparrow} = \frac{\partial}{\partial\tilde{\nu}}(\tilde{\nu}\epsilon_{xc}) + (1-\zeta)\frac{\partial}{\partial\zeta}\epsilon_{xc}$$
$$V_{xc,\downarrow} = \frac{\partial}{\partial\tilde{\nu}}(\tilde{\nu}\epsilon_{xc}) - (1+\zeta)\frac{\partial}{\partial\zeta}\epsilon_{xc}. \quad (6)$$

In the magnetic field the exchange and correlation energy density is interpolated between the infinite and the no-field limits as[21]

$$\epsilon_{xc}^B(\tilde{\nu},\zeta) = \epsilon_{xc}^\infty(\tilde{\nu})e^{-f(\tilde{\nu})} + \epsilon_{xc}^0(\tilde{\nu},\zeta)(1-e^{-f(\tilde{\nu})}), \quad (7)$$

with $f(\tilde{\nu}) = (3\tilde{\nu}/2) + 7\tilde{\nu}^4$ and $\epsilon_{xc}^\infty(\tilde{\nu}) = -0.782\sqrt{\tilde{\nu}}e^2/(kl)$. The low-field energy functional is interpolated between the spin-polarized and the unpolarized limits[22]

$$\epsilon_{xc}^0(\tilde{\nu},\zeta) = \epsilon_{xc}(\tilde{\nu},0) + f^i(\zeta)\left[\epsilon_{xc}(\tilde{\nu},1) - \epsilon_{xc}(\tilde{\nu},0)\right]$$
$$\text{with} \quad f^i(\zeta) = \frac{(1+\zeta)^{3/2} + (1-\zeta)^{3/2} - 2}{2^{3/2}-2}. \quad (8)$$

The exchange and correlation contributions are then separated $\epsilon_{xc}(\tilde{\nu},\zeta) = \epsilon_x(\tilde{\nu},\zeta) + \epsilon_c(\tilde{\nu},\zeta)$, and the exchange contribution for the unpolarized system is expressed as $\epsilon_x(\tilde{\nu},0) = -[4/(3\pi)]\sqrt{\tilde{\nu}}e^2/(kl)$, while for the polarized one it is $\epsilon_x(\tilde{\nu},1) = -[4/(3\pi)]\sqrt{2\tilde{\nu}}e^2/(kl)$. We use the parameterization of Ceperley and Tanatar for the correlation contribution[23]

$$\epsilon_c(\tilde{\nu},\zeta) = a_0\frac{1+a_1x}{1+a_1x+a_2x^2+a_3x^3}E_{Ryd}^*, \quad (9)$$

where $x = \sqrt{r_s} = (2/\tilde{\nu})^{1/4}(a/a_B^*)^{1/2}$, and a_B^* is the effective Bohr radius. The optimized values of the correlation parameters a_i have been found by Ceperley and Tanatar using a Monte Carlo model of a 2DEG.[23]

So stated, the $V_{xc,\sigma}$'s are complicated functionals of the the spin densities, or $\tilde{\nu}$ and ζ, and thus a common method is to solve the resulting Kohn-Sham equations on a spatial grid. We instead follow the alternative example of a number of researchers to use the mathematical basis $\{|\alpha\rangle\}$ to cast the LSDA functionals into matrix expressions in order to implement a grid-free LSDA.[15,16,17,18] Briefly, the method relies on the following steps: In the end we need the matrix elements of the exchange and correlation potentials, $\langle\alpha|V_{{\rm xc},\sigma}|\beta\rangle$, so we start by constructing $\langle\alpha|\tilde{\nu}|\beta\rangle$. The polarization ζ has to be treated as a combination of two functions, $f = \tilde{\nu}_\uparrow - \tilde{\nu}_\downarrow$ and $g = \tilde{\nu}^{-1}$. Due to the completeness of the basis we then have $\langle\alpha|\zeta|\beta\rangle = \sum_\gamma\langle\alpha|f|\gamma\rangle\langle\gamma|g|\beta\rangle$, and to evaluate the latter matrix elements we need to find a unitary matrix $\mathbf{U}$ that diagonalizes the matrix $\tilde{\nu}$, i.e. $\tilde{\nu} = \mathbf{U}\,\mathbf{diag}(\lambda_1,\cdots,\lambda_n)\mathbf{U}^+$, where λ_i are the eigenvalues of $\tilde{\nu}$. All functions of the matrix $\tilde{\nu}$ are now calculated according to

$$f[\tilde{\nu}] = \mathbf{U}\,\mathbf{diag}\left(f(\lambda_1),\cdots,f(\lambda_n)\right)\mathbf{U}^+. \quad (10)$$

Corresponding methods are used for more complex functionals of $\tilde{\nu}$ and ζ.

The matrix elements of the electron density n or the effective filling factor $\tilde{\nu}$ can be written in terms of a generalized one-electron overlap integral and the matrix elements of the density operator ρ

$$\langle\alpha|\tilde{\nu}|\beta\rangle = \sum_{p,q}\rho_{qp}\int d\mathbf{r}\;\phi_\alpha^*(\mathbf{r})\phi_p^*(\mathbf{r})\phi_q(\mathbf{r})\phi_\beta(\mathbf{r}). \quad (11)$$

In the ground state the density matrix is constructed from the expansion coefficients of electronic states in terms of the basis states, the occupation of the states expressed by the Fermi distribution, and the chemical potential μ ensuring the conservation of the number of electrons, $\rho_{qp} = \sum_\gamma f(\varepsilon_\gamma - \mu) c^*_{\gamma p} c_{\gamma q}$. We use here the density matrix ρ_{qp} in anticipation of the situation when the system will be subjected to a strong external time-dependent perturbation and quantities like the single-electron energy spectrum, and the occupation described by the Fermi distribution will have no meaning. The analytic expression for the generalized one-electron overlap integral can be found in Appendix. The matrix elements of the direct Coulomb interaction and the confinement potential have been published elsewhere.[24,25]

B. Time-dependent excitation

At $t = t_0$ the Hamiltonian of the system acquires time dependence, $H(t) = H + W(t)$, caused by an external perturbation of a finite duration

$$\begin{aligned} W(t) &= V_t r^{|N_p|} \cos(N_p \phi) \exp(-sr^2 - \Gamma t) \\ &\quad \sin(\omega_1 t) \sin(\omega t) \theta(\pi - \omega_1 t). \end{aligned} \tag{12}$$

Since the perturbation is of arbitrary strength we have to assume the task of solving the equation of motion for the density operator

$$i\hbar d_t \rho(t) = [H + W(t), \rho(t)]. \tag{13}$$

The structure of this equation is inconvenient for numerical evaluation so we resort instead to the time-evolution operator T, defined by $\rho(t) = T(t)\rho_0 T^+(t)$, which has simpler equation of motion

$$\begin{aligned} i\hbar \dot{T}(t) &= H(t)T(t) \\ -i\hbar \dot{T}^+(t) &= T^+(t)H(t). \end{aligned} \tag{14}$$

In each time step the density operator ρ changes and thus also the DFT Hamiltonian which is a functional of ρ. Similar nonlinear problem is encountered when the time-dependent Kohn-Sham equations are solved directly on a spatial grid.[9] We apply a similar procedure here discretizing time and using the Crank-Nicholson algorithm for the time integration resulting in the coupled equations

$$\begin{aligned} &\rho(t + \Delta t) = T(\Delta t)\rho(t)T^+(\Delta t) \\ &\left\{1 + \frac{i\Delta t}{2\hbar} H[\rho; t + \Delta t]\right\} T(\Delta t) \approx \left\{1 - \frac{i\Delta t}{2\hbar} H[\rho; t]\right\}, \end{aligned} \tag{15}$$

with the initial condition, $T(0) = 1$, already used on the right hand side of (15). In each time-step the equations have to be iterated until self-consistency is attained. This is performed in the truncated Fock-Darwin basis $\{|\alpha\rangle\}$ for the corresponding matrix version of the equations (15).

The accuracy and the fine-tuning of the model has been tested for the ground state with comparison to the exact results calculated for a circular parabolically confined quantum dot,[26] and in the time-evolution by convincing us that the model can reproduce the Kohn results for the absorption of a Far-infrared radiation.[27,28] In addition, the normalization condition for the density matrix is tested regularly during the integration of the time-dependent problem.

C. Specification of model parameters

In order to model a short GaAs quantum wire with or without an embedded impurity and several electrons we select the parameters, $\hbar\omega_0 = 3.37$ meV, and assume $g^* = 0.44$, and $m^* = 0.067m$. The impurity potential is selected to be Gaussian (2) with $V_0 = -10$ meV, and $a^2\gamma = 1.0$. The Gaussian shape is used here in order to limit the size of the basis during the CPU-intensive time integration of the problem. The wire shape of the system is attained by setting $\alpha_2 = -0.7$ and $\alpha_i = 0$ for all $i \neq 2$. The charge density for 10 electrons in the system is shown in Fig. 1 with and without an embedded impurity. At $B = 0$ T the length of the system is approximately 200nm, and the difference between the charge densities with and without an impurity in the system turns up in Fig. 1b as a fairly well localized impurity state. This can

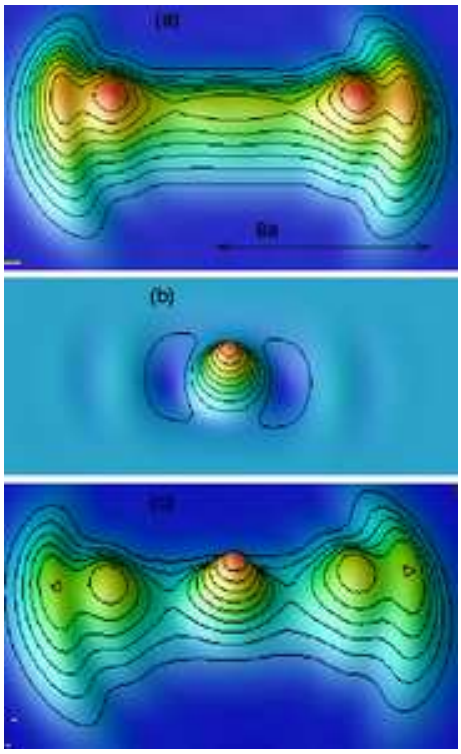

FIG. 1: Color online. The electron density of the interacting system without an impurity (a), the difference in the electron density of system with and without an impurity (b), and the density for a system with an impurity (c). $B = 0$ T, $V_0 = -10$ meV, $T = 1$ K, $N = 10$, and $a \approx 13$ nm.

be confirmed by the Kohn-Sham energy spectra displayed

in Fig. 2, where the main change due to the addition of the impurity potential into the system is the lowering of the energy of the highest almost degenerate doubly occupied state by approximately 1 meV. The calculations

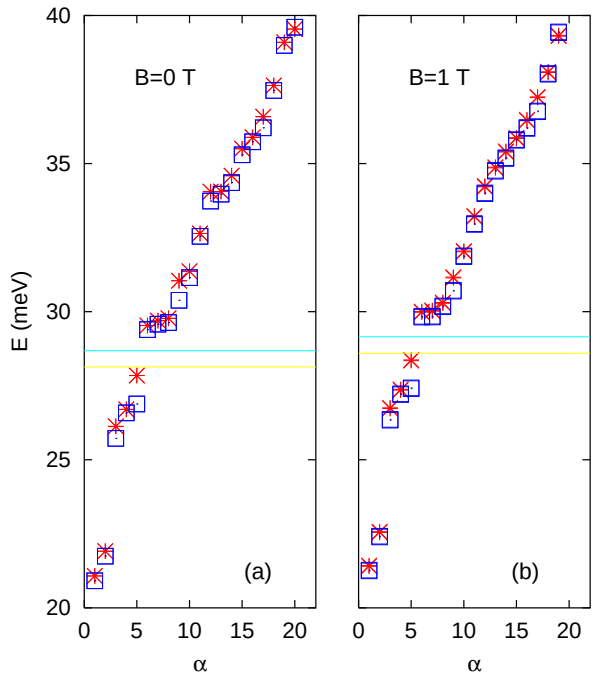

FIG. 2: Color online. The Kohn-Sham single-electron energy spectra for the interacting electron system with (□) and without (∗) an impurity for $B = 0$ T (a), and $B = 1$ T (b). The integer α is a quantum number labeling the states. The lower horizontal line (yellow) represents the chemical potential μ for system with an impurity, and the higher one (blue) indicates μ for a system without an impurity. $T = 1$ K and $N = 10$.

reported here are for $B = 0$ T, and $B = 1$ T. In order to avoid numerical problems with the determination of the eigenvectors for exactly degenerate eigenvalues in the diagonalization of the Hamiltonian we actually use $B = 10^{-8}$ T instead of $B = 0$ T.

For the radiation pulse (12) of duration just over 3 ps,[1] we select $\Gamma = 2$ ps^{-1}. The envelope frequency corresponds to $\hbar\omega_1 = 0.658$ meV, and the base frequency is equivalent to $\hbar\omega = 2.63$ meV. Meanwhile, we select a $|N_p| = 1$ and $s = 0$ in (12) to represent a dipole radiation. But, due to the finite cut-off in the basis $|\alpha\rangle$ the matrix elements of the excitation can never be purely of the dipole type. We choose the orientation of the initial radiation pulse (12) to be either parallel, $\parallel$, to the long axis of the system or perpendicular to it, $\perp$. The finite asymmetric cut-off of the basis can introduce a tiny mixing of the perpendicular and the parallel excitation at vanishing magnetic field. In fact, the basis cut-off is performed by specifying the highest radial quantum number $n_{\max}$ used in the calculation, by doing so an asymmetry is introduced between the number of negative and positive angular quantum numbers M. This asymmetry is made unimportant with respect to the energy spectrum and the wave functions of the system by selecting a high enough $n_{\max}$, but the representation of a dipole potential is not quite so clean. A simple alternative method is not easy since the effective asymmetry does depend on the magnetic field.

We integrate the equations for the time-evolution operator (15) over a time interval of 50 ps using an increment $\Delta t = 0.0025$ ps and evaluate the expectation values for the coordinates x and y for each spin direction, $\langle x\rangle_\uparrow$, etc. We can thus identify oscillations perpendicular or parallel to the long axis of the system, talking about perpendicular or parallel detection. Resonances in the collective oscillations of the electron spin densities are sought by Fourier transformation of the time series in the interval $5 - 50$ ps, when the external excitation has been turned off and switch-on effects have vanished and the system has reached a "steady state".

III. RESULTS

A. The $B = 0$ T case

In Fig. 3 the Fourier power spectra of the time series for the coordinates x and y are used to represent the excitation spectra of the system without an impurity. The $\parallel$ polarized excitation is seen to introduce a tiny $\perp$ oscillation (1/10 the amplitude) as has been explained earlier, but at the same frequency. This simple excitation spectrum does not change much with increasing excitation strength V_t. A second harmonic shows up in the parallel oscillation, but more interestingly the height of the main peak does not grow linearly with the excitation strength when $V_t a > 1$ meV. The excitation then becomes nonlinear and as $V_t a = 5$ meV we see that it shifts slightly to lower energy. Before commenting on the red shift of the peak with increasing V_t we show what happens in the system with an embedded impurity in Fig. 4. The main peak in the longitudinal oscillation (Fig. 4b) is slightly blue shifted compared to the system with no impurity. The reason is readily explained by a glance at the Kohn-Sham energy spectra in Fig. 2; the presence of the impurity potential enlarges the energy gap around the chemical potential μ. Instead of a spatially fairly extended state just below μ there is now a localized state at lowered energy. Again, with increasing excitation strength V_t we see a red shift of the resonance in the parallel oscillations. At strong excitation we can not refer back to the Kohn-Sham spectra of the ground state, but we can expect that the energy pumped into the system makes the states just below the gap more extended, thus reducing the effective energy gap. The perpendicular oscillation in Fig. 4a is more complex than before. Again, there is a resonance at the same energy as in the parallel mode that is slightly red shifted with increased excitation, but there now appear resonances at higher

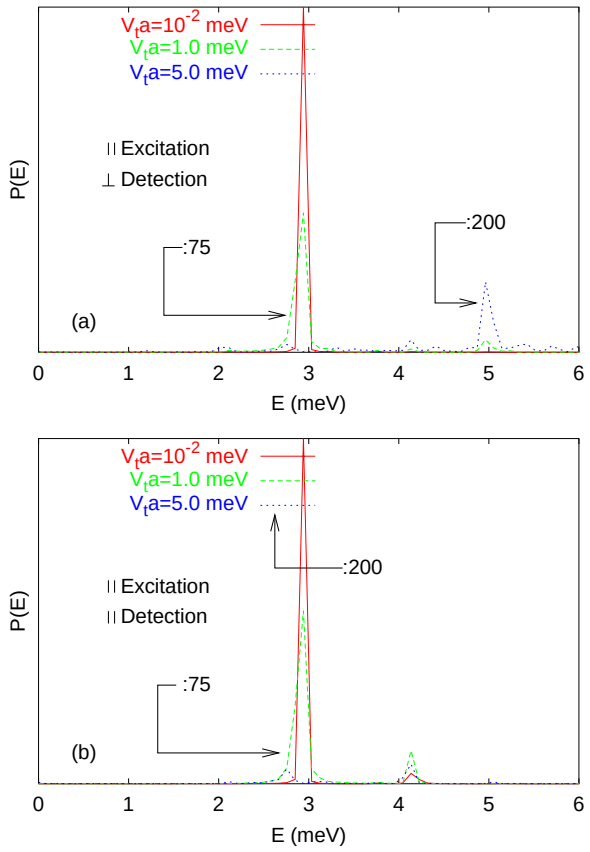

FIG. 3: Color online. The Fourier power spectrum of the time series for the expectation values of the coordinates perpendicular (⊥) (a), and parallel (||) (b) to the long axis of the system. The excitation is ***parallel*** to the same axis. Division factors for the stronger excitations are indicated in the figure. ***No impurity*** is in the system. $B = 0$ T, $T = 1$ K, and $N = 10$.

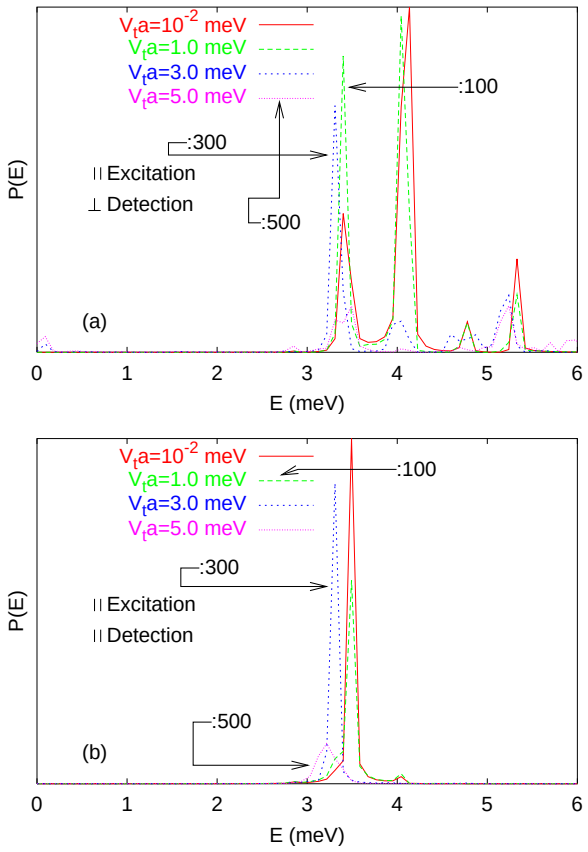

FIG. 4: Color online. The Fourier power spectrum of the time series for the expectation values of the coordinates perpendicular (⊥) (a), and parallel (||) (b) to the long axis of the system. The excitation is ***parallel*** to the same axis. Division factors for the stronger excitations are indicated in the figure. ***Impurity is present*** in the system. $B = 0$ T, $T = 1$ K, and $N = 10$.

energies indicating the presence of more localized modes in the system, an extra excitation mode located at the impurity site. This is again supported by a look at the Kohn-Sham energy spectra in Fig. 2a, at the changes just above the gap caused by the impurity.

The case of the initial excitation pulse aligned perpendicular with the long axis is review in Fig. 5. We see that again in the ⊥ detection we have the peak structure encountered in Fig. 4a as could be expected, but the slight presence of a ∥ excitation in the initial pulse is not of the dipole kind so mostly higher order modes are excited in the ∥ direction. Exactly this, is further displayed in Fig. 6a, where, in addition, the relative strength of the response is also visible. In contrast, the strong confinement in the perpendicular direction of the system or the wire ensures the ⊥ response to be not strongly dependent on the main excitation polarization, see Fig. 6b.

To clearly demonstrate the collective oscillations in the system we show in Fig. 7 the induced electron density for the system with and without an embedded impurity for the two polarizations of the excitation pulse. The two figures Fig. 7a and b for the ⊥ excitation show that the ends of the system oscillate in the ⊥ direction while the oscillation around the impurity is at least at this moment parallel to the long axis. In case of no impurity in the system the oscillation of the center part is more perpendicular. When the excitation is applied ∥ to the system (see Figs. 7c and d) the main oscillation mode is also along the system of the fundamental dipole type as can be seen by comparing the induced density to the total density in Fig. 1. In this case the oscillation seems to be more extended to the whole system when there is an impurity present in it, but when there is no impurity present the center of the system displays a tiny bit of a ⊥ mode superimposed on its motion. In fact, the induced density can show higher order oscillation modes that we can not discern with our time series of the expectations values for the the coordinates x and y, which are most sensitive to dipole oscillations occuring in the system.[7,9]

The red shift of the collective resonance for the system

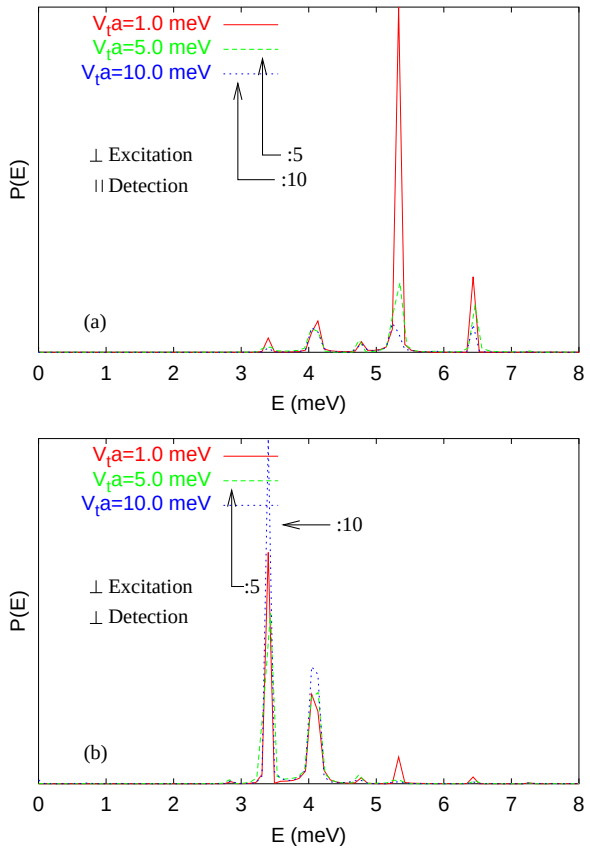

FIG. 5: Color online. The Fourier power spectrum of the time series for the expectation values of the coordinates perpendicular ($\perp$) (a), and parallel ($\parallel$) (b) to the long axis of the system. The excitation is ***perpendicular*** to the same axis. Division factors for the stronger excitations are indicated in the figure. ***Impurity is present*** in the system. $B = 0$ T, $T = 1$ K, and $N = 10$.

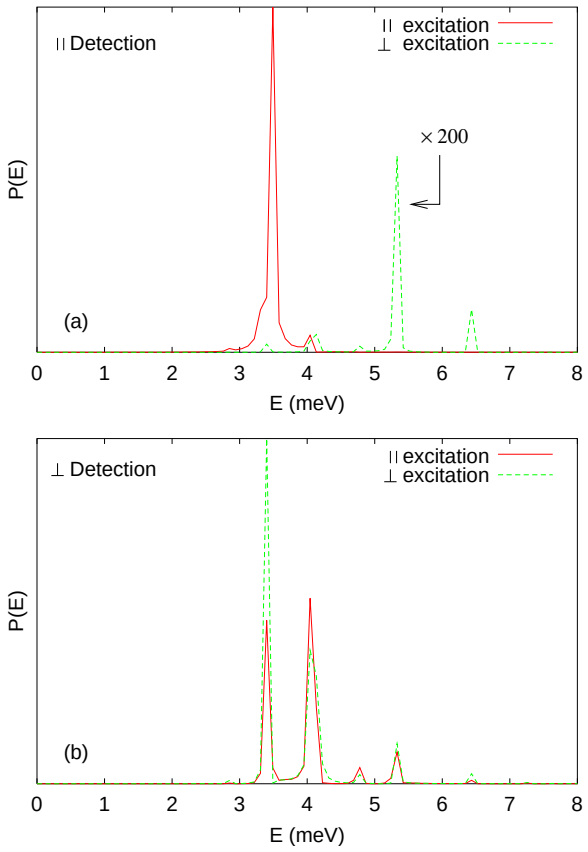

FIG. 6: Color online. Comparison of the Fourier power spectrum of the time series for the expectation values of the coordinates parallel ($\parallel$) (a), and perpendicular ($\perp$) (b) to the long axis of the system in the case of an excitation ***perpendicular*** or ***parallel*** to the same axis. A multiplication factor is indicated in the figure. ***Impurity is present*** in the system. $V_t a = 1.0$ meV, $B = 0$ T, $T = 1$ K, and $N = 10$.

with an embedded impurity is further explored in Fig. 8 in comparison with the response of the system without an impurity. Clearly, the resonance is red shifted and broadened with increasing excitation strength V_t pointing towards a reduction in the binding energy of the impurity.

Comparison between the sub figures of Fig. 8 reveals that with increasing excitation strength more energy flows into a simple dipole oscillation of the system when an impurity is present in it. This is confirmed by the induced electron density in this case showing large oscillations of the electron density around the impurity site parallel to the system, and mostly in harmony with the oscillations in the rest of the system, reflected in a single resonance. The broadening of the resonance is indicative of a finer structure that we are unable to resolve in our calculations.

The case is different with the perpendicular oscillation shown in Fig. 9, where in the end a strong excitation will lead to many modes becoming active. So, even though the parallel collective oscillation remains simple the perpendicular one is generally more complex.

B. The $B = 1$ T case

The collective oscillations in the finite magnetic field $B = 1$ T are for short times after the initial excitation pulse very similar to the oscillations encountered in the system in no magnetic field as could be guessed by comparing the Kohn-Sham energy spectra for the two cases, see Fig. 2. It has though to be kept in mind that the Lorentz force now ensures a quick communication between the parallel and the perpendicular modes, they are not independent. But more happens: The finite size of the system together with the small Zeeman energy, and the finite temperature $T = 1$ K establish a tiny spin polarization in the ground state, i.e. the two spin densities do not have exactly the same spatial dependence.

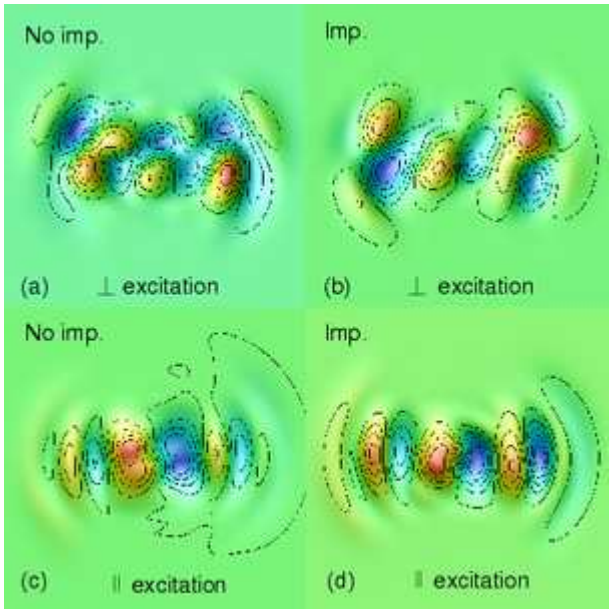

FIG. 7: Color online. The induced density at time $t = 50$ ps for $\perp$ excitation for a system without (a), and with an impurity (b), and for $\parallel$ excitation without (c), and with an impurity (d). The excitation strength $V_t a = 1.0$ meV (a), 5.0 meV (b) 10^{-2} meV (c), 1.0 meV (d). $B = 0$ T, $T = 1$ K, and $N = 10$.

The spatially varying exchange force in the LSDA gives a different restoring force to the spin densities. All these factors lead to a slow flow of energy into the individual oscillations of the spin densities as can be seen in Fig. 10. This flow is so slow that after 50 ps the system has still not entered a "steady state" as in the case of $B = 0$ T. We are still observing switch-on effects for the collective oscillations of the spin densities after 50 ps. In the spin oscillation we see present both high and low frequency components but the lack of a steady state prevents us from making a Fourier analysis. Just to avoid any misconception we should mention that the time increment of $\Delta t = 0.0025$ ps gives us 20,000 points in the range of 50 ps and at a finer level of resolution the spin oscillation looks very smooth with no apparent noise like might be hastily inferred by looking at Fig. 10.

Even more amazing is the fact that to begin with this spin oscillation increases with the strength of the excitation V_t but, as is seen in Fig. 10, for a still stronger excitation it again *decreases*. Stronger excitation of the system prevents the energy in flowing into the collective spin oscillations, but directs it to the center-of-mass motion and the other collective charge oscillations. This behavior is definitely a nonlinear phenomena that can not be observed in a model of linear response.

The presence of the impurity also quite effectively directs more energy into the spin oscillation as is seen in Fig. 10. This can be explained by a stronger spatial variation of the exchange force around the impurity.

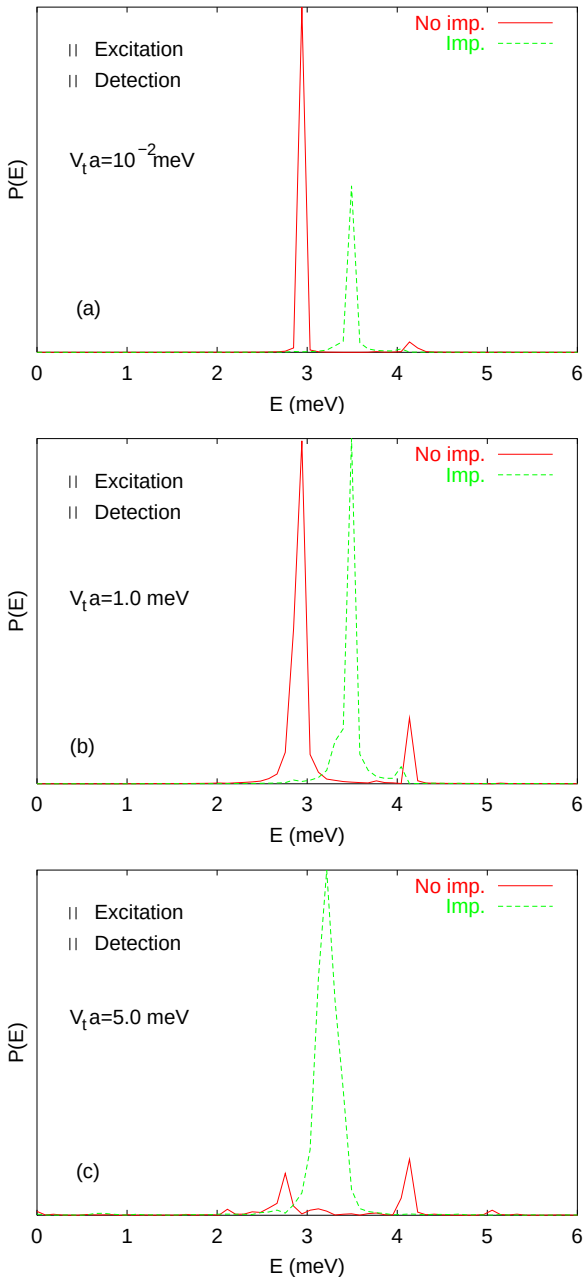

FIG. 8: Color online. The Fourier power spectrum of the time series for the expectation values of the coordinate parallel ($\parallel$) to the long axis of the system with or without an impurity in the case of an excitation along the same axis. $B = 0$ T, $T = 1$ K, and $N = 10$.

The regularity of the collective spin oscillations can be seen in Fig. 11 where simply both spin densities are seen almost overlapping at $t = 50$ ps. The peak structure of the spin densities closely follows the structure of the ground state charge density displayed in Fig. 1.

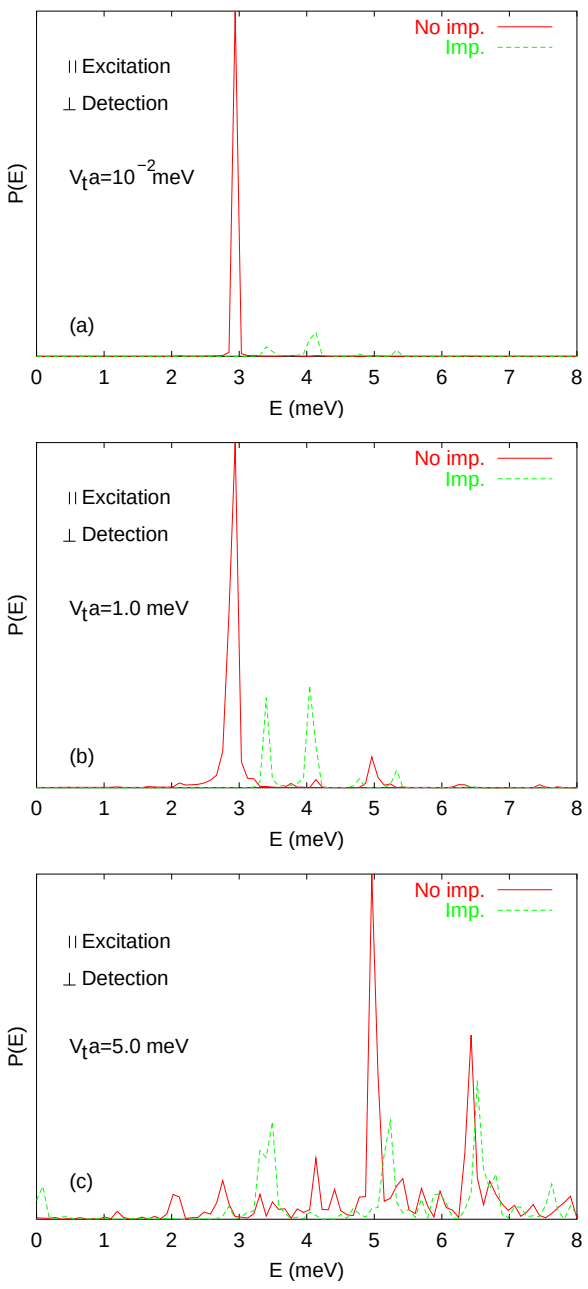

FIG. 9: Color online. The Fourier power spectrum of the time series for the expectation values of the coordinate perpendicular (⊥) to the long axis of the system with or without an impurity in the case of an excitation along the same axis. $B = 0$ T, $T = 1$ K, and $N = 10$.

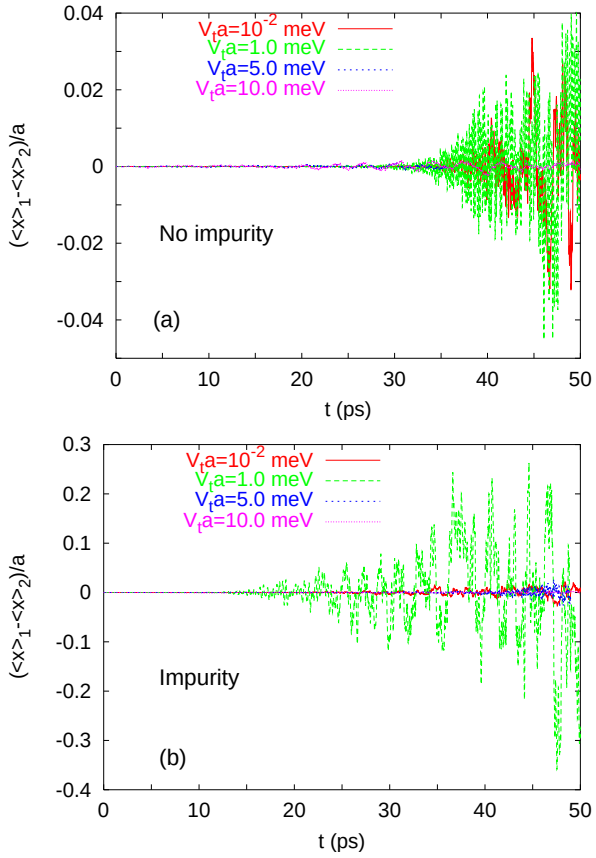

FIG. 10: Color online. The time evolution of spin oscillations, characterized by $(\langle x\rangle_\downarrow - \langle x\rangle_\uparrow)/a$, for a system without (a) and with (b) an impurity. $\Delta t = 0.0025$ ps, $B = 1$ T, $T = 1$ K, and $N = 10$.

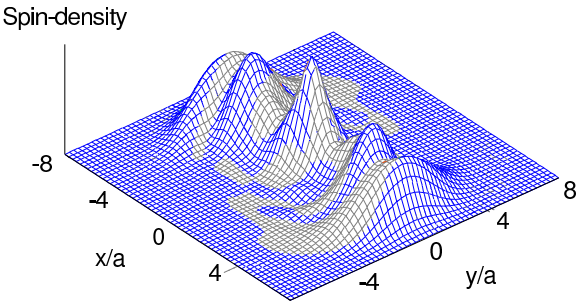

FIG. 11: Color online. The two components of the spin density at the time point $t = 50$ ps in a system with an impurity. The spin densities are very similar in shape and are superimposed here on one another with different shades. $V_t a = 10^{-2}$ meV, $B = 1$ T, $T = 1$ K, and $N = 10$.

IV. DISCUSSION AND SUMMARY

Without the external magnetic field present the collective charge oscillations excited in the system by the short THz pulse do reach a "steady state" condition within 1 or 2 picoseconds after the excitation is switched off allowing a Fourier analyzes to discern the modes present.

At low excitation level we observe a linear regime, but at higher excitation nonlinear effects show up. The excitation gap in the system is reduced indicating a less localized single-electron states and in particular the effective binding energy of the impurity is reduced.

At finite magnetic field ($B = 1$ T) a slowly increasing collective oscillation of the spin densities has not reached a "steady state" condition after 50 ps. As the spin oscillation is directly coupled with the collective charge oscillations a Fourier analyses is not possible in this case for either component. The excitation of the collective spin oscillations is much more effective when an impurity is present in the system, since then the initial spin densities at $t = 0$ have a larger spatial variation. The more amazing fact is that with increased intensity of the initial excitation the onset of the spin oscillation can be effectively shut down. We contribute this to the flow of the energy nonadiabatially pumped into the system being more easily directed to the oscillations of the charge density in this case.

For the results shown in this paper we have always used the same type of excitation pulse. What would happen if we use a longer pulse with several oscillations or of a different form. We can not claim that we have thoroughly investigated this question, but our limited experimenting with this seems to indicate that the pulse form is indeed important for the heights of the resonance peaks, but does not affect their location strongly. We are pumping energy into the system by the excitation in varying amounts depending on the peak shape and duration and it can be expected that this also affects the initial distribution of the energy between the modes. By removing the system further from equilibrium than we do we are sure that stronger nonlinear effects can occur with considerable change of peak locations also. We already see the precursors of this in the redshift of the peaks connected to the impurity embedded in the system.

We are aware that our choice of an impurity potential represented by a Gaussian well does not correspond to unscreened Coulomb impurities that might be situated in the plane of the 2DEG in a nanosystems. This form has only been selected in order to keep the truncation of the Fock-Darwin basis within reasonable bounds in order to enable the "long-time" integration of the time evolution operator to extend to 50 ps with 20,000 steps, within each one the self-consistency was attained with further 4 loops to properly update the density operator. With these requirements in mind it should be reiterated that the present model was not designed to describe any known experimental device, but rather it was constructed to give qualitative insight into time-dependent phenomena that can take place in a nanosystem that is irradiated by short and intensive THz pulse, in response to the preparations underway in several experimental groups to study these phenomena. We only study the behavior of the system for a short time after the application of the excitation and neglect all possible damping and dissipation effects that would be caused by the coupling of the system to its immediate environment. These are certainly very important effects that await further investigation.

Acknowledgments

The research was partly funded by the Icelandic Natural Science Foundation, the University of Iceland Research Fund, the National Science Council of Taiwan under Grant No. 91-2119-M-007-004, and the National Center for Theoretical Sciences, Tsing Hua University, Hsinchu Taiwan. VG acknowledges instructive discussions with Llorens Serra and a beneficial exchange of programming ideas with Ingibjörg Magnúsdóttir and Gabriel Vasile.

THE GENERALIZED ONE-ELECTRON OVERLAP INTEGRAL

In order to reduce the memory size needed to store the generalized overlap integral it is convenient to split it into two parts by applying the completeness of the basis once

$$\Phi_{\alpha pq\beta} = \int d\mathbf{r}\ \phi^*_\alpha(\mathbf{r})\phi^*_p(\mathbf{r})\phi_q(\mathbf{r})\phi_\beta(\mathbf{r}) = \sum_\delta \Phi_{\alpha p\delta}\Phi_{q\beta\delta}, \tag{16}$$

where an analytic expression for the wave functions corresponding to the Fock-Darwin basis states $|\alpha\rangle = |M_\alpha, n_\alpha\rangle$ gives

$$\Phi_{\alpha p\delta} = 2\pi a^2\ \delta_{M_\alpha+M_p,M_\delta}\ \beta_\alpha\beta_p\beta_\delta\ 2^{(|M_\alpha|+|M_\beta|+|M_\delta|)/2}$$
$$\sum_{i_\alpha=0}^{n_\alpha}\sum_{i_p=0}^{n_p}\sum_{i_\delta=0}^{n_\delta}\frac{(-1)^{i_\alpha+i_p+i_\delta}}{i_\alpha!i_p!i_\delta!}\binom{n_\alpha+|M_\alpha|}{n_\alpha-i_\alpha}\binom{n_p+|M_p|}{n_p-i_p}$$
$$\binom{n_\delta+|M_\delta|}{n_\delta-i_\delta}\left(\frac{|M_\alpha|+|M_\beta|+|M_\delta|}{2}+i_\alpha+i_p+i_\delta\right)!$$
$$\times\left(\frac{2}{3}\right)^{[(|M_\alpha|+|M_\beta|+|M_\delta|)/2]+i_\alpha+i_p+i_\delta+1},$$

with

$$\beta_\alpha = \frac{1}{2^{(|M_\alpha|+1)/2}}\sqrt{\frac{n_\alpha!}{\pi(|M_\alpha|+n_\alpha)}}. \tag{17}$$

* Permanent address: Science Institute, University of Iceland, Dunhaga 3, IS-107 Reykjavik, Iceland

[1] P. C. M. Planken, P. C. van Son, J. N. Hovenier, T. O. Klaassen, W. T. Wenckebach, B. N. Murdin, and G. M. H.

Knippels, Phys. Rev. B **51**, 9643 (1995).
[2] J. L. Nie, W. Xu, and L. B. Lin (2003), cond-mat/03044258.
[3] R. G. Mani, J. H. Smet, K. von Klitzing, V. Narayanamurti, W. B. Johnson, and V. Umansky, Nature **420**, 646 (2002).
[4] A. Lorke, R. J. Luyken, A. O. Govorov, J. P. Kotthaus, J. M. Garcia, and P. M. Petroff, Phys. Rev. Lett. **84**, 2223 (2000).
[5] M. Abo-Bakr, J. Feikes, K. Holldack, P. Kuske, W. B. Peatman, U. Schade, and G. Wstefeld, Phys. Rev. Lett. **90**, 094801 (2003).
[6] X. Chu and S.-I. Chu, Phys. Rev. A **63**, 023411 (2001).
[7] A. Puente, L. Serra, and V. Gudmundsson, Phys. Rev. B **64**, 235324 (2001).
[8] V. Gudmundsson, C.-S. Tang, and A. Manolescu, Phys. Rev. B **67**, 161301(R) (2003).
[9] A. Puente and L. Serra, Phys. Rev. Letters **83**, 3266 (1999).
[10] Z. Qian, A. Constantinescu, and G. Vignale, Phys. Rev. Lett. **90**, 066402 (2003).
[11] F. Aryasetiawan and O. Gunnarsson, Phys. Rev. B **66**, 165119 (2002).
[12] G. Vignale and M. Rasolt, Phys. Rev. Lett. **59**, 2360 (1987).
[13] A. D. Bandrauk and H. Z. Lu, Phys. Rev. A **62**, 053406 (2000).
[14] X. Chu and S.-I. Chu, Phys. Rev. A **64**, 063404 (2001).
[15] Y. C. Zheng and J. Almlöf, Chem. Phys. Letters **214**, 397 (1993).
[16] K. R. Glaesemann and M. S. Gordon, Journal of Chem. Phys. **108**, 9959 (1998).
[17] K. R. Glaesemann and M. S. Gordon, Journal of Chem. Phys. **110**, 6580 (1999).
[18] G. Berghold, J. Hutter, and M. Parrinello, Theor. Chem. Acc. **99**, 344 (1998).
[19] V. Fock, Z. Phys. **47**, 446 (1928).
[20] M. I. Lubin, O. Heinonen, and M. D. Johnson, Phys. Rev. B **56**, 10373 (1997).
[21] M. Koskinen, M. Manninen, and S. M. Reimann, Phys. Rev. Lett. **79**, 1389 (1997).
[22] U. von Barth and B. Holm, Phys. Rev. B **54**, 8411 (1996).
[23] B. Tanatar and D. M. Ceperley, Phys. Rev. B **39**, 5005 (1989).
[24] I. Magnúsdóttir, Master's thesis, Háskóli Íslands, http://www.raunvis.hi.is/reports/1999/RH-08-99.html (1999).
[25] G. Vasile, Master's thesis, Háskóli Íslands, http://www.raunvis.hi.is/reports/2002/RH-18-2002.html (2002).
[26] D. Pfannkuche, V. Gudmundsson, and P. Maksym, Phys. Rev. B **47**, 2244 (1993).
[27] P. A. Maksym and T. Chakraborty, Phys. Rev. Lett **65**, 108 (1990).
[28] V. Gudmundsson and R. Gerhardts, Phys. Rev. B **43**, 12098 (1991).